

RSC Advances



This is an *Accepted Manuscript*, which has been through the Royal Society of Chemistry peer review process and has been accepted for publication.

Accepted Manuscripts are published online shortly after acceptance, before technical editing, formatting and proof reading. Using this free service, authors can make their results available to the community, in citable form, before we publish the edited article. This *Accepted Manuscript* will be replaced by the edited, formatted and paginated article as soon as this is available.

You can find more information about *Accepted Manuscripts* in the [Information for Authors](#).

Please note that technical editing may introduce minor changes to the text and/or graphics, which may alter content. The journal's standard [Terms & Conditions](#) and the [Ethical guidelines](#) still apply. In no event shall the Royal Society of Chemistry be held responsible for any errors or omissions in this *Accepted Manuscript* or any consequences arising from the use of any information it contains.

Mercury thioarsenate glasses: a hybrid chain/pyramidal network †

Mohammad Kassem,^{ab} Sohayb Khaoulani,^{ab} Arnaud Cuisset,^{ab} David Le Coq,^c
Pascal Masselin^{ab} and Eugene Bychkov^{*ab}

^a *Univ Lille Nord de France, F-59000 Lille, France*

^b *ULCO, LPCA, EA CNRS 4493, F-59140 Dunkerque, France*

^c *Sciences Chimiques de Rennes, UMR CNRS 6226, Eq. Verres et Céramiques,
Univ. de Rennes I, F-35042 Rennes, France*

Abstract

Very little is known about mercury chalcogenide glasses. Using Raman spectroscopy and DFT modelling, we show that the $(\text{HgS})_x(\text{As}_2\text{S}_3)_{1-x}$ glasses, $0.0 \leq x \leq 0.5$, form a hybrid Hg-S chain/As-S pyramidal network, highly unusual for metal chalcogenide glasses. This network is evidenced by Hg-S stretching modes at 300 and 370 cm^{-1} and an As-S spectral envelope centred at 340 cm^{-1} . The decreasing glass transition temperature is consistent with a gradual substitution of more rigid corner-sharing CS- $\text{AsS}_{3/2}$ pyramids by flexible $(\text{HgS}_{2/2})_n$ chain fragments. Nevertheless we cannot exclude completely the presence of a small fraction of $\text{HgS}_{4/4}$ tetrahedral units. A non-monotonic change in electronic transport properties and metacinnabar β -HgS traces detected using neutron diffraction in large $x = 0.5$ samples support the dual structural role of mercury.

* Email: bychkov@univ-littoral.fr

† Electronic supplementary information (ESI) available: Electrical characteristics of HgS- As_2S_3 glasses (Table S1); Raw Raman spectra and background correction (Fig. S1); Visualisation of Hg-S stretching modes in Hg_2S_3 oligomer (Movies SM1-SM3)

1 Introduction

Chalcogenide and chalcogen halide glasses have attracted a great deal of interest in both fundamental research and technological fields. They are suitable model systems to verify theories of glass formation, network rigidity, ionic and electronic transport in disordered systems, *etc.*¹⁻⁴ The extensive glass forming regions with many elements of the Periodic Table makes it possible to change the composition of these glasses over a wide range thus modifying significantly their electrical, magnetic, optical, thermal, chemical and other properties. Consequently, the functional chalcogenide glass materials appear to be suitable for various solid-state devices and a large number of advanced applications: (1) phase-change optical recording in rewritable high-density storage media,⁵⁻⁷ (2) vitreous electrolytes for all-solid-state batteries in rechargeable power systems,^{8,9} (3) chemical sensors for environmental monitoring and industrial process control,^{10,11} (4) integrated optics and photonic applications.¹²⁻¹⁴ Chalcogenide glasses transparent in the far IR region ($\lambda > 15 \mu\text{m}$) are critically important for many optical systems. Selective remote IR spectroscopy of various biotoxin and gas species, thermal imaging, interstellar IR detection of life signature at exoplanetary systems, *etc.*¹⁵⁻¹⁸ represent only a few examples. The glasses containing heavy elements are particularly promising for these applications. Surprisingly, very little is known about the structure and properties of mercury chalcogenide glasses except for a few papers with approximate glass-forming regions and basic glass characterisation.¹⁹⁻²¹ In particular, the question arises whether mercury will modify the pyramidal network of arsenic chalcogenide or tetrahedral network of germanium chalcogenide glasses. Dimorphism of crystalline mercury sulphide (chain-like cinnabar α -HgS vs. cubic metacinnabar β -HgS with zinc-blende lattice) also opens discussions on local mercury environment in the glass and its structural role in the network. In this paper, using Raman spectroscopy and DFT modelling, we report a hybrid Hg-S chain/As-S pyramidal network in the HgS-As₂S₃ quasi-binary system, highly unusual for metal chalcogenide glasses. The reduced network connectivity related to a gradual substitution of more rigid corner-sharing CS-AsS_{3/2} pyramids by flexible (HgS_{2/2})_n chain fragments is responsible for thermal properties of the mercury thioarsenate glasses. The dual structural role of mercury will also be discussed in relation to non-monotonic changes in electronic transport properties of these glassy insulators.

2 Experimental

2.1 Glass preparation

The quasi-binary (HgS)_x(As₂S₃)_{1-x} samples ($x = 0.0, 0.1, 0.2, 0.3, 0.4, 0.5, 0.6$) were prepared from HgS and As₂S₃. Red mercury sulphide α -HgS (99.99% pure, Sigma-Aldrich) was used for synthesis of HgS-As₂S₃ samples without additional purification. Arsenic sulphide As₂S₃ was prepared from arsenic pieces (99.9999 % pure, Cerac) and sulphur pellets (99.9999% pure, Acros Organics). Arsenic and sulphur were purified from As₂O₃ and SO₂ oxides at the surface by heating under vacuum at 320 °C and 130 °C,

respectively. The detailed synthesis and homogenisation procedure was described elsewhere.²² Sample compositions (typically 3 g of the total mass), in required proportions, were sealed under vacuum (10^{-6} mbar) in silica tubes (8 mm ID/10 mm OD) and heated to 850 °C before quenching from 800 °C into a cold salt/water mixture.

All the samples were characterised by laboratory x-ray diffraction (XRD) using a Bruker D8 Advance diffractometer and Cu K_{α} radiation at ambient conditions. For selected samples with high mercury sulphide content, $0.4 \leq x \leq 0.5$, the time-of-flight neutron diffraction (ND) and high-energy x-ray scattering (HE-XRD) have been used. The ND measurements have been carried out using the NOMAD diffractometer at the Spallation Neutron Source (Oak-Ridge National Laboratory, TN, USA). The 11ID-B and 6ID-D instruments at the Advanced Photon Source (Argonne National Laboratory, IL, USA) were used for the HE-XRD experiments.

2.2 Density and DSC measurements

The density, d , of the samples was measured by a hydrostatic method using toluene as an immersion fluid and a germanium standard (5.323 g cm^{-3}). A Sartorius YDK 01-0D density kit was used for the measurements. The differential scanning calorimetry (DSC) experiments were carried out using a TA Q200 instrument at a heating rate of 10 K min^{-1} in the temperature range from 20 to 400 °C. Samples of 10 to 15 mg, encapsulated in a standard aluminium pan, were used for DSC measurements. An empty aluminium pan was served as a reference, and high purity nitrogen N_2 as the purge gas. DSC traces were used to obtain the glass transition temperature, T_g , as the temperature corresponding to the intersection of two linear portions adjoining the transition elbow of the DSC trace. Further details of glass characterisation techniques were reported previously.^{22,23}

2.3 Conductivity measurements

The DC electrical conductivity of the samples, σ_{dc} , was measured using a Hewlett Packard 4339B high resistance meter with an applied voltage of 100 volts. A temperature range between 65 and 155-185 °C was used, depending on composition; the maximum temperature was below T_g for the glass samples. The quenched samples, prepared as rectangular plates, were polished using SiC powder (9.3μ grain size). The sample sides were ground parallel and gold was deposited on opposite sides to form electrodes for conductivity experiment, *i.e.*, the electrochemical cell for conductivity measurements was Au|glass|Au. Typical thickness of the samples was in the range of 1.0-1.2 mm. The temperature dependence of conductivity was studied in several cycles, each consisting of a heating and a cooling step, in order to investigate a possible hysteresis. The hysteresis effect was found to be insignificant.

2.4 Raman spectroscopy measurements

Raman spectra were collected at room temperature using a LABRAM Dilor spectrometer (Jobin Yvon Horiba Group) equipped with a triple monochromator, liquid nitrogen cooled CCD detector and a microscope. Raman scattering was excited by a 632.8 nm He-Ne laser and recorded in the 80-1200 cm^{-1} spectral range. To avoid crystallisation of the glassy samples, the laser power was set to 0.1 mW and the acquisition time varied between 60 and 150 s. Two to four spectra were registered for each sample at different positions in order to verify the sample homogeneity and the absence of photo-induced phenomena. The spectrometer resolution was 1cm^{-1} .

2.5 DFT modelling

The DFT calculations have been carried out using GAUSSIAN 09²⁴ associated with its graphical user interface GaussView. In order to find a compromise between the cost of the calculations and the accuracy of the results, structural optimisation and harmonic vibrational frequency calculations were performed for size-limited clusters composed of $\text{Hg}_2\text{S}_3(\text{H}_2)$ and $\text{Hg}_4\text{S}_5(\text{H}_2)$ oligomeric chains, as well as of $\text{HgAs}_2\text{S}_6(\text{H}_4)$ and $\text{Hg}_2\text{As}_2\text{S}_7(\text{H}_4)$ chain/pyramidal subunits. Our previous DFT modelling of the chalcogenide glass vibrational properties²⁵ has shown that the above cluster size is sufficient to adequately represent the characteristic vibration modes in the glass and follow compositional trends. In particular case of mercury thioarsenate glasses, the $\text{Hg}_2\text{S}_3(\text{H}_2)$ cluster appears to be the smallest Hg-S chain fragment representing the helical geometry in α -HgS. The next oligomer $\text{Hg}_4\text{S}_5(\text{H}_2)$ was chosen to study the effect of chain length on vibrational properties. The hybrid units $\text{HgAs}_2\text{S}_6(\text{H}_4)$ and $\text{Hg}_2\text{As}_2\text{S}_7(\text{H}_4)$ reflect the effect of asymmetric bonding, *i.e.*, =As-S-Hg-, in a hypothetical continuous glass network on the vibrational force constants compared to pure Hg-S chains, -Hg-S-Hg-. Terminal protons (H_m), where $m = 2$ or 4, added to the bridging sulphur species in the clusters to avoid dangling bonds, will be omitted in further structural discussions as well as the respective hydrogen-related vibrations.

The DFT calculations were carried out with the Becke²⁶ three parameters hybrid exchange functional and the Lee-Yang-Parr correlation functional (B3LYP).²⁷ The rather large 6-311G++(3df,2p) basis-set was used for arsenic, sulphur and hydrogen. In the case of atoms with a heavy nucleus like mercury, relativistic effects due to the inner core electrons having a velocity close to the speed of light should be taken into account. For Hg atoms, we have declared in the input file an external pseudo-potential or Effective Core Potential available in the Environment Molecular Science Library.²⁸ The small-core relativistic pseudo-potential basis set (cc-pVTZ-PP)²⁹ was specifically employed. All the structures were optimised using the tight convergence option ensuring adequate convergence and reliability of computed wavenumbers. In the tight convergence option, the average root mean square (RMS) force on all atoms was set to be 1×10^{-5} atomic units and scales the maximum remaining force on an atom in the system, the maximum displacement as well as the average RMS change over all structural parameters

accordingly.²⁴ Harmonic frequency calculations were performed with the method and basis set used for the optimisation. The best quality of the wavenumber predictions was obtained with an optimum scaling factor close to 1 and a root-mean square standard deviation around 5 cm^{-1} .³⁰

In the following sections we will present and discuss only the calculated vibrational and geometric properties. The electronic properties (HOMO – LUMO gap, charges on atoms, *etc.*) are omitted from the analyses since we do not have the respective experimental data for comparison.

3 Results and discussion

3.1 Glass forming range

Visually, the $(\text{HgS})_x(\text{As}_2\text{S}_3)_{1-x}$ samples containing less than 60 mol.% HgS appear to be vitreous. The $x = 0.5$ composition synthesised in small quantities (0.1-0.3 g) does not show any Bragg peaks, Fig. 1(a), while a large sample (3 g) exhibits small but distinct Bragg peaks corresponding to cubic metacinnabar β -HgS, Fig. 1(b). The high-temperature β -HgS form is metastable at ambient conditions and seems to be quenched from the melt in the large $x = 0.5$ sample. The glassy/crystalline $x = 0.6$ sample shows both broad diffraction features characteristic of glassy and amorphous materials and intense and narrow Bragg peaks related to trigonal cinnabar α -HgS, Fig. 1(c).

The glass-forming range in the HgS-As₂S₃ system at $x \leq 0.5$, obtained in our conditions of glass synthesis and quenching, is similar to the results reported earlier.²¹ The observed rather high maximum mercury content in the glass ($x = 0.5$ or 14.3 at.% Hg) represents a significant improvement when compared to the other quasi-binary thioarsenate systems Hg-As₂S₃³¹ and HgI₂-As₂S₃.³² The limiting mercury concentration in the Hg-As₂S₃ glasses was reported to be ≈ 2 at.% Hg, while in the HgI₂-As₂S₃ system, it does not exceed ≈ 5 at.% Hg.

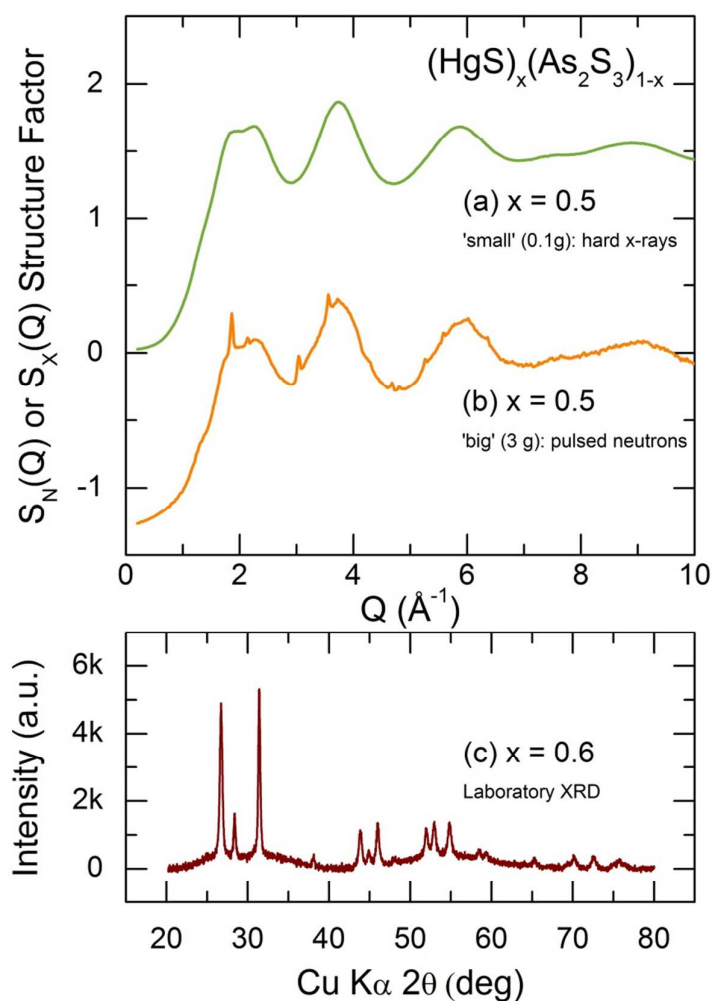


Fig. 1 Low- Q part of the (a) x-ray $S_x(Q)$ and (b) neutron $S_N(Q)$ structure factors for a 'small' (0.1 g) and 'big' (3 g) $(\text{HgS})_{0.5}(\text{As}_2\text{S}_3)_{0.5}$ samples measured using high-energy x-ray scattering and pulsed neutron diffraction, respectively; (c) XRD pattern of the glassy/crystalline $(\text{HgS})_{0.6}(\text{As}_2\text{S}_3)_{0.4}$ sample. The observed Bragg peaks for the 'big' $(\text{HgS})_{0.5}(\text{As}_2\text{S}_3)_{0.5}$ sample correspond to cubic metacinnabar β -HgS; those for $(\text{HgS})_{0.6}(\text{As}_2\text{S}_3)_{0.4}$ are related to trigonal cinnabar α -HgS crystallites.

3.2 Density and thermal properties

The density of glassy samples in the $(\text{HgS})_x(\text{As}_2\text{S}_3)_{1-x}$ system increases monotonically with x while the mean atomic volume remains essentially invariant (Fig. 2). This trend persists even with partial crystallisation of the quasi-binary compositions at $x \geq 0.5$. The density increase in the HgS- As_2S_3 system is expected since the two crystalline forms of mercury sulphide have significantly higher density ($d_{\alpha\text{-HgS}} = 8.17 \text{ g cm}^{-3}$ and $d_{\beta\text{-HgS}} = 7.70 \text{ g cm}^{-3}$)^{33,34} than the As_2S_3 host glass ($d_{g\text{-As}_2\text{S}_3} = 3.18 \text{ g cm}^{-3}$) or crystalline orpiment As_2S_3 ($d_{c\text{-As}_2\text{S}_3} = 3.46 \text{ g cm}^{-3}$).³⁵

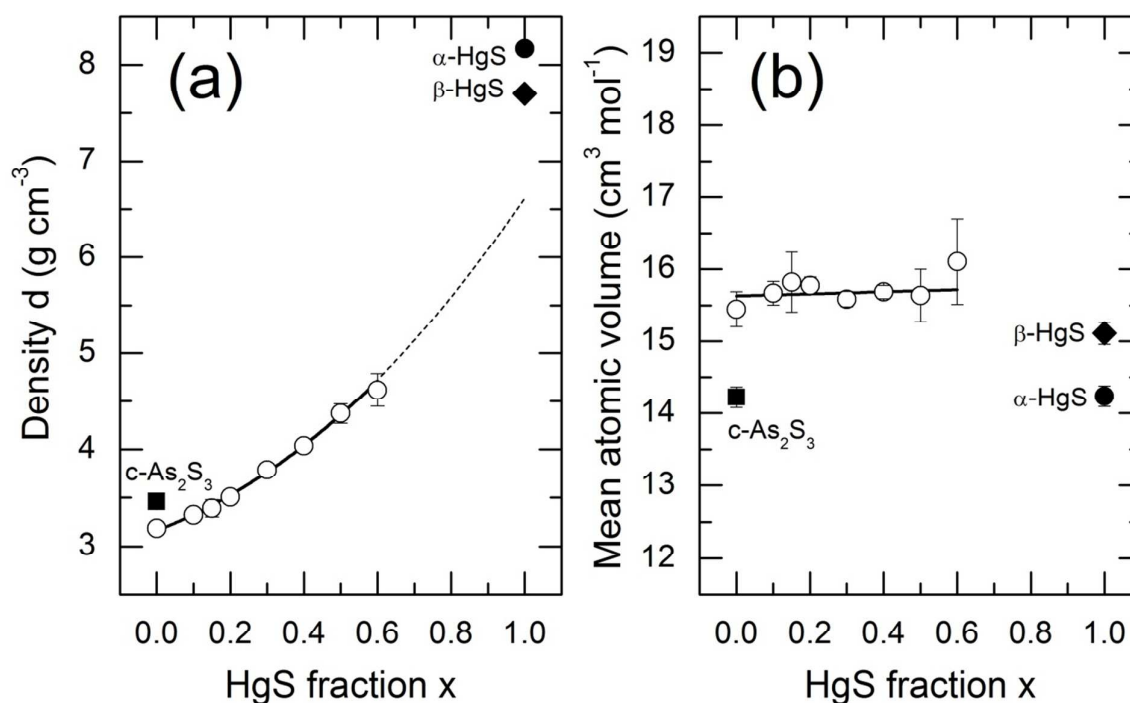


Fig. 2 (a) Density and (b) mean atomic volume of the $(\text{HgS})_x(\text{As}_2\text{S}_3)_{1-x}$ alloys as a function of the mercury sulphide content. The $x = 0.5$ and 0.6 samples are partially crystallised. The respective parameters of crystalline orpiment c -As₂S₃³⁵ and the mercury sulphide polymorphs^{33,34} are also shown.

DSC traces of the $(\text{HgS})_x(\text{As}_2\text{S}_3)_{1-x}$ glasses are plotted in Fig. 3. All the samples show a single endothermic step-like feature corresponding to glass transition. The single glass transition as well as the absence of small-angle x-ray and neutron scattering at the scattering vector $Q < 0.5 \text{ \AA}^{-1}$, Fig. 1, indicates a homogeneous glass nature on both macroscopic and mesoscopic scale. For the HgS-rich glasses, the T_g feature is followed either by a weak and broad ($x = 0.4$) or sharp and intense ($x = 0.5$) exothermic crystallisation peak, whose maximum at T_x shifts to lower temperatures, reflecting the reduced glass-forming ability.

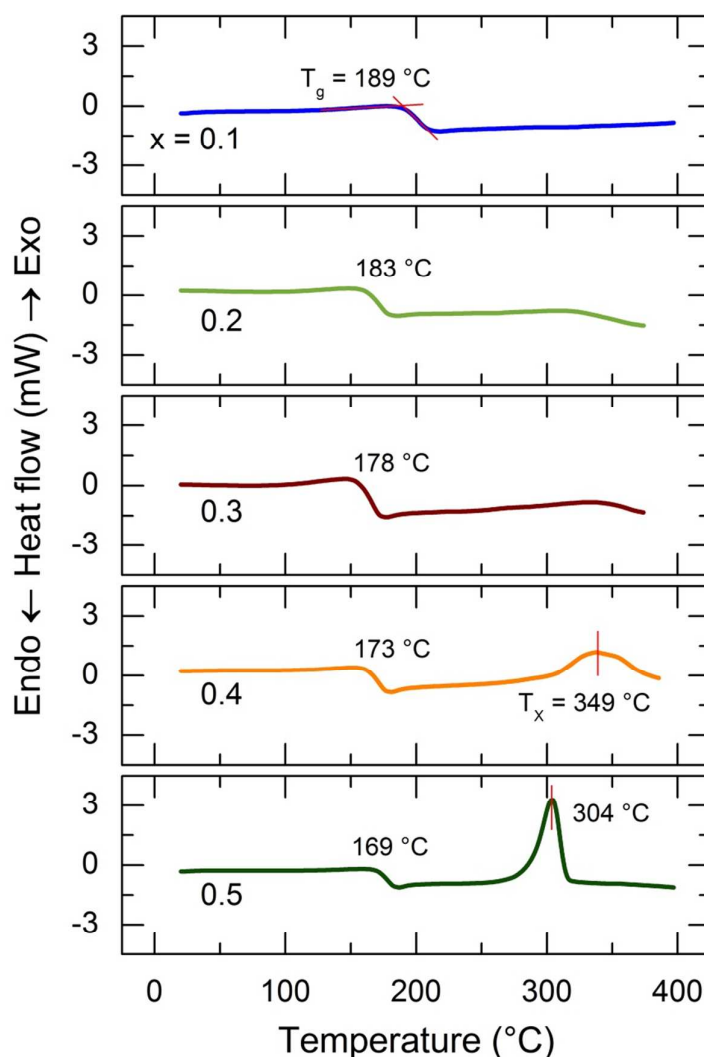


Fig. 3 DSC traces of the $(\text{HgS})_x(\text{As}_2\text{S}_3)_{1-x}$ glasses, $0.1 \leq x \leq 0.5$, obtained in the temperature range from 20 to 400 °C.

The glass transition temperature T_g in the mercury thioarsenate glasses decreases with x from 197 °C to 169 °C, Fig. 4(a). It should be noted that similar $(\text{PbS})_x(\text{As}_2\text{S}_3)_{1-x}$ vitreous alloys are characterised by a rather constant or slightly increasing T_g ,^{36,37} also shown in Fig. 4(a). The reduced connectivity in the mercury thioarsenate glasses seems to be responsible for the observed changes. Figure 4(b) reproduces the glass transition temperature in vitreous HgS-As₂S₃ as a function of the arsenic atomic fraction y together with the thermal properties of homogeneous sulphur-rich As_{*y*}S_{1-*y*} binaries, $y \leq 0.4$.³⁸ In the latter system, the excessive sulphur species at $y < 0.4$ form S-S dimers and/or short oligomeric sulphur chains replacing bridging sulphur in corner-sharing CS-AsS_{3/2} pyramids, thus reducing the network connectivity and decreasing the glass transition temperature.³⁸⁻⁴⁰ The T_g composition dependence in glassy HgS-As₂S₃ mimics this trend.

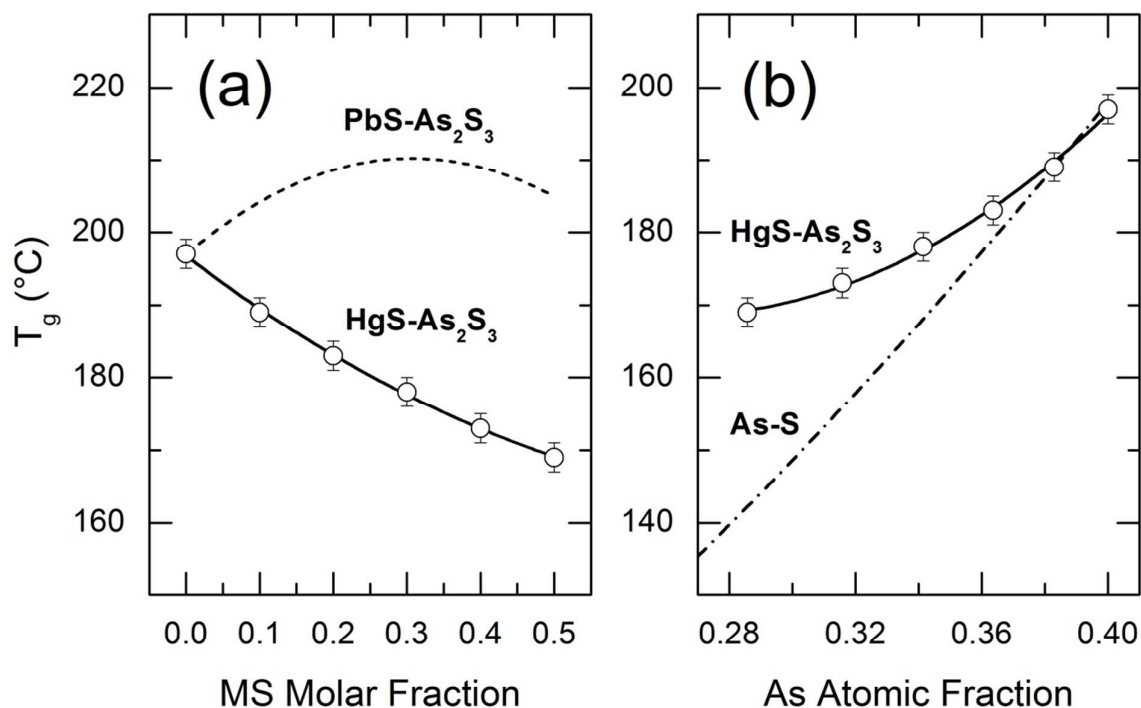


Fig. 4 Composition dependence of the glass transition temperature T_g in the quasi-binary system $(\text{HgS})_x(\text{As}_2\text{S}_3)_{1-x}$; (a) comparison with $(\text{PbS})_x(\text{As}_2\text{S}_3)_{1-x}$ (the dashed line),^{36,37} (b) comparison with homogeneous sulphur-rich As-S binaries (the dash-dotted line).³⁸ The solid lines are drawn as a guide to the eye.

3.3 Electric transport

Typical temperature dependencies of the DC conductivity for the $\text{HgS-As}_2\text{S}_3$ glasses are shown in Fig. 5. They do not show any significant hysteresis effects and obey the Arrhenius law:

$$\sigma_{dc}(T) = \sigma_0/T \exp(-E_\sigma/kT), \quad (1)$$

where σ_0 is the pre-exponential factor, E_σ the activation energy, k the Boltzmann constant, and T the temperature. The room-temperature conductivity σ_{298} , E_σ and σ_0 were calculated from a least-square fit of the data to eqn. (1). The results are listed in Table S1 (electronic supplementary information) and displayed in Fig. 6.

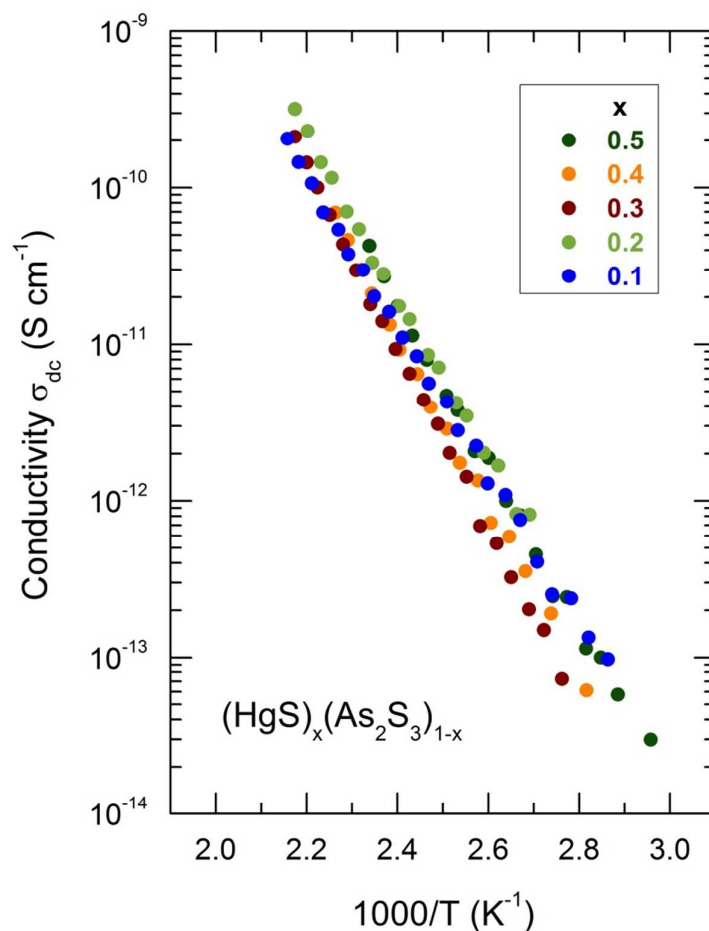


Fig. 5 Temperature dependence of the DC electrical conductivity σ_{dc} for the quasi-binary $(\text{HgS})_x(\text{As}_2\text{S}_3)_{1-x}$ glassy system.

Both the $\sigma_{dc}(x, T)$ temperature dependence, Fig. 5, and the conductivity isotherm $\sigma_{298}(x)$, Fig. 6(a), show that the mercury thioarsenate glasses are electronic insulators, $3 \times 10^{-17} \text{ S cm}^{-1} \leq \sigma_{298}(x) \leq 5 \times 10^{-16} \text{ S cm}^{-1}$. The conductivity activation energy, $E_\sigma \approx \frac{1}{2} E_g$, where E_g is the optical gap, also remains nearly invariant, changing between 0.97 and 1.18 eV. The conductivity pre-exponential factor, $10^4 \text{ S cm}^{-1} \text{ K} \leq \sigma_0(x) \leq 10^6 \text{ S cm}^{-1} \text{ K}$, indicates that the electronic transport in the $(\text{HgS})_x(\text{As}_2\text{S}_3)_{1-x}$ glasses involves the extended electronic states in the top of the valence band and/or at the bottom of the conduction band.³ We should note a non-monotonic behaviour of the conductivity parameters as a function of the mercury sulphide content x . The room-temperature conductivity $\sigma_{298}(x)$ exhibits a shallow minimum and the activation energy $E_\sigma(x)$ a distinct maximum at $x \approx 0.3$ with subsequent systematic changes at higher x .

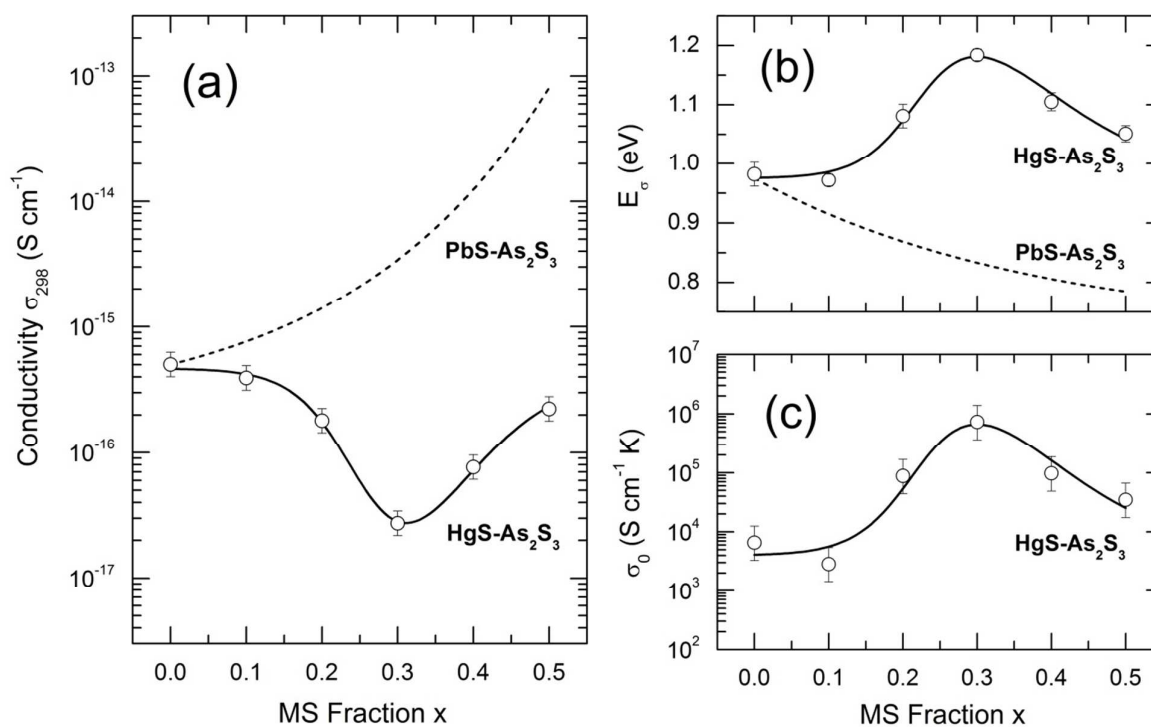


Fig. 6 (a) Room-temperature conductivity σ_{298} , (b) conductivity activation energy E_σ , and (c) pre-exponential factor σ_0 for the quasi-binary $(\text{HgS})_x(\text{As}_2\text{S}_3)_{1-x}$ glass system. The conductivity parameters for glassy As_2S_3 were taken from Ref. 19. The solid lines are drawn as a guide to the eye. The average conductivity parameters for $(\text{PbS})_x(\text{As}_2\text{S}_3)_{1-x}$ glasses^{37,41,42} are also shown by the dashed lines.

The observed conductivity changes appear to be different from those in lead thioarsenate glassy system $(\text{PbS})_x(\text{As}_2\text{S}_3)_{1-x}$.^{37,41,42} A monotonic increase of $\sigma_{298}(x)$ by two orders of magnitude with simultaneous decrease of the conductivity activation energy by 0.2 eV was reported for $\text{PbS-As}_2\text{S}_3$, also shown in Fig. 6. These continuous changes in electronic transport properties were attributed to a narrow optical gap of semiconducting lead sulphide ($E_g = 0.3$ eV)^{41,42} compared to a wide gap of the electronic insulator As_2S_3 ($E_g = 2.0\text{-}2.4$ eV).³ In contrast, the two polymorphic forms of mercury sulphide show drastically different electronic properties. Red cinnabar α -HgS is electronic insulator ($E_g = 2.1$ eV)⁴³ while black metacinnabar β -HgS belongs to narrow-gap semiconductors ($E_g = 0.4$ eV).⁴⁴ It seems that polymorphic nature of HgS is responsible for non-monotonic DC electrical conductivity of the mercury thioarsenate glasses.

3.4 Raman spectra

The measured raw Raman spectra of the $(\text{HgS})_x(\text{As}_2\text{S}_3)_{1-x}$ glasses show a drastic decrease in the Raman intensity below 150 cm^{-1} , related to the instrument function of the spectrometer (Fig. S1 in ESI). Consequently, the majority of bending and deformation

modes at low frequencies, $\omega < 200 \text{ cm}^{-1}$, escape from observation. In the high-frequency region above 500 cm^{-1} , only a weak second-order Raman feature at $\omega \approx 700 \text{ cm}^{-1}$ appears to be visible. Therefore, we will focus our attention on the $200\text{-}600 \text{ cm}^{-1}$ domain describing and analysing the stretching features in this range. In order to allow a direct quantitative comparison of the Raman spectra for different glass compositions, a Voigt function was used to fit the spectral background and then subtracted from the experimental data with subsequent normalisation to the most intense peak (Fig. S1, ESI).

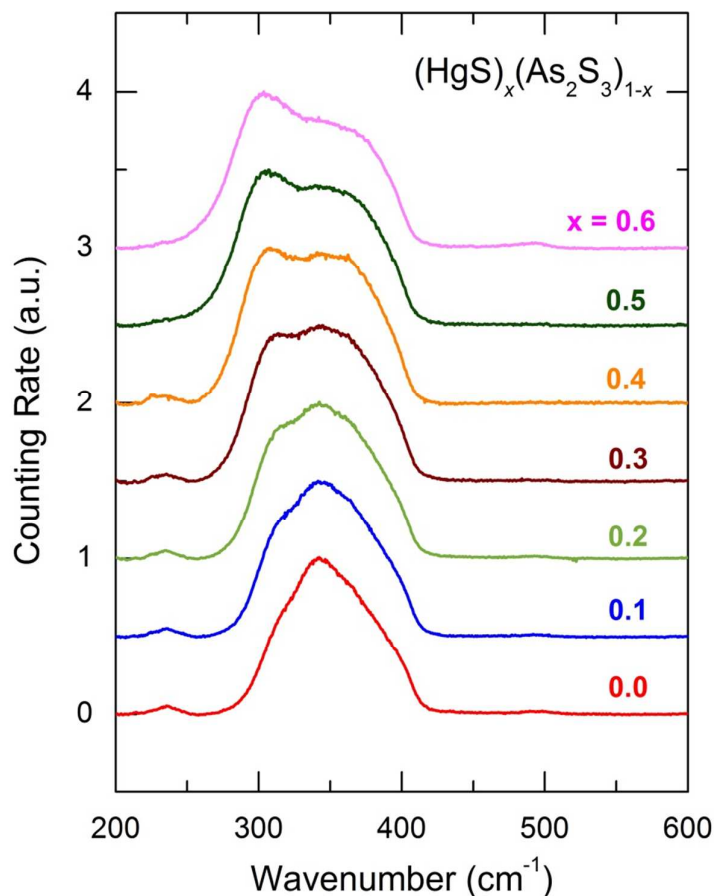


Fig. 7 Normalised and background corrected Raman spectra of the $(\text{HgS})_x(\text{As}_2\text{S}_3)_{1-x}$ alloys. See text for further details.

The resulting Raman spectra of the $(\text{HgS})_x(\text{As}_2\text{S}_3)_{1-x}$ glasses are displayed in Fig. 7. As expected, the As_2S_3 host glass ($x = 0.0$) exhibits a broad poorly resolved multimodal feature centred at 340 cm^{-1} corresponding to symmetric and asymmetric As-S stretching modes in corner-sharing $\text{AsS}_{3/2}$ pyramids and As-S-As bridges.^{38,45-49} Two additional weak but distinct features at 235 cm^{-1} and 495 cm^{-1} , also reported by many researchers,⁴⁸⁻⁵² are related to As-As and S-S stretching, respectively. These modes come from different structural units either with homopolar As-As or S-S bonds and indicate a small degree of chemical disorder in stoichiometric As_2S_3 (2-3 % according to

Refs. 50,51). The 235 cm^{-1} and 495 cm^{-1} modes are decreasing monotonically with x as well as the main 340 cm^{-1} feature. Instead, a new mode appears at $\approx 310\text{ cm}^{-1}$, first as a shoulder, increases in intensity, shifts to lower frequencies and becomes predominant at $x \geq 0.4$. As a result, the full spectral width at half maximum (FWHM) increases by 30-40 % compared to As_2S_3 . In addition to the 300 cm^{-1} feature, the second less intense shoulder appears at about 370 cm^{-1} . Since the two peaks are increasing in intensity with x , we attribute them to mercury sulphide additions.

Direct fitting of poorly resolved multimodal Raman spectra without a detailed DFT modelling of the vibrational properties for *all* possible structural fragments in the glass represents a difficult task. For example, the C_s symmetry of the AsS_3 pyramid in monoclinic orpiment As_2S_3 ³⁵ suggests already three different As-S stretching modes: symmetric and asymmetric stretch for two identical As-S bonds, $2.296 \pm 0.009\text{ \AA}$, and a single stretch for a shorter bond, $2.257 \pm 0.019\text{ \AA}$. The corner-sharing bipyramidal unit $\text{CS-As}_2\text{S}_5$ has 5 different As-S stretching frequencies between 326 and 371 cm^{-1} , *etc.*⁵³

As a first approximation to reveal the structural role of mercury sulphide in the thioarsenate glasses, we have subtracted the scaled Raman signal, corresponding to glassy As_2S_3 , from the Raman spectra of quasi-binary glasses. Typical subtraction procedure is shown in Fig. 8(a), the resulting difference spectra are presented in Fig. 8(b).

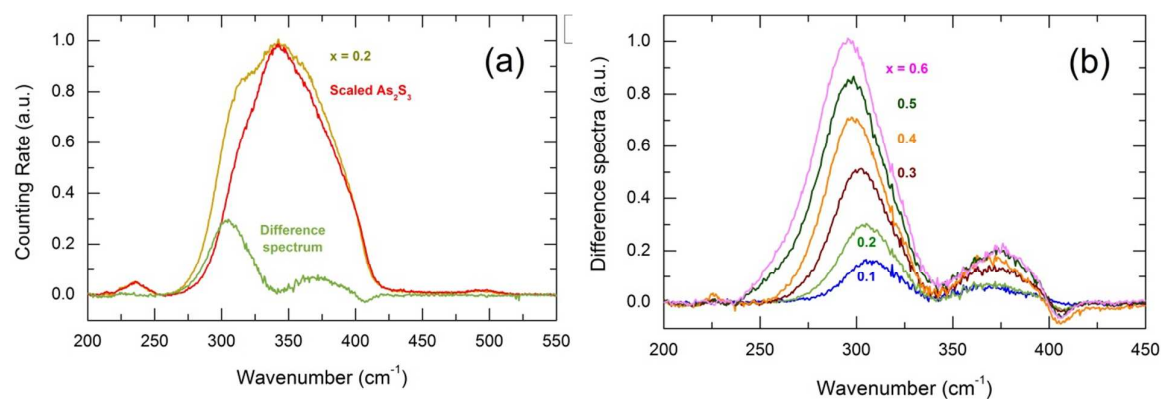


Fig. 8 (a) Subtraction procedure for the $x = 0.2$ glass and the resulting difference spectrum $I_{x=0.2}(\omega) - k_{\text{As}_2\text{S}_3} \times I_{\text{As}_2\text{S}_3}(\omega)$; (b) the difference spectra for the $(\text{HgS})_x(\text{As}_2\text{S}_3)_{1-x}$ glasses divided by $k_{\text{As}_2\text{S}_3}$, *i.e.*, normalised to a constant As_2S_3 spectral envelope. The numbers in Fig. 8(b) denote the mercury sulphide fraction in the glass.

The subtraction confirms the appearance of two major features in the $(\text{HgS})_x(\text{As}_2\text{S}_3)_{1-x}$ glasses: (i) at $300\text{-}310\text{ cm}^{-1}$, and (ii) at $\approx 370\text{ cm}^{-1}$. The intensity of both broad spectral components increases with x . The spectral shape of the As_2S_3 envelope at high frequencies, $360\text{ cm}^{-1} \leq \omega \leq 420\text{ cm}^{-1}$, seems to be changing in the mercury thioarsenate glasses, evidenced by a negative amplitude in the difference spectra at $\approx 405\text{ cm}^{-1}$. This

change will affect both the spectral shape and intensity of the minor HgS-related mode at $\approx 370\text{ cm}^{-1}$. On the contrary, we do not expect any significant distortions for the peak at $\approx 300\text{ cm}^{-1}$.

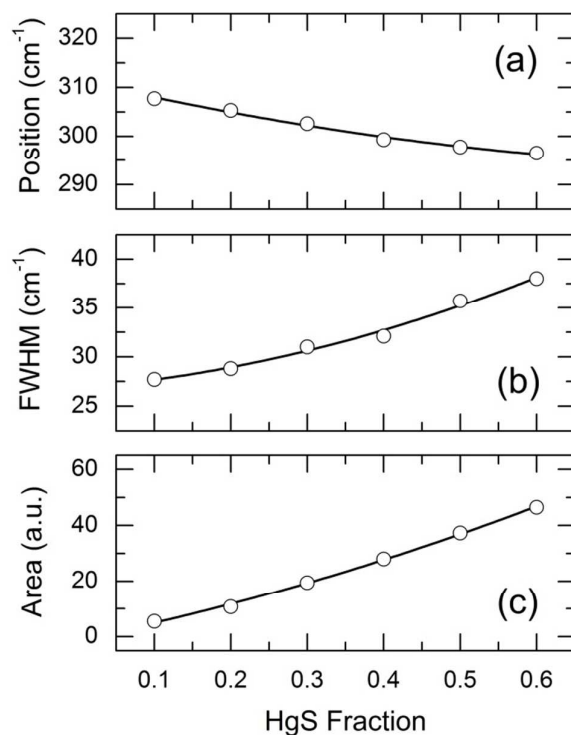


Fig. 9 (a) Peak position, (b) full-width at half maximum (FWHM), and (c) relative area of the Hg-S stretching feature at $\approx 300\text{ cm}^{-1}$ in the $(\text{HgS})_x(\text{As}_2\text{S}_3)_{1-x}$ glasses. The solid lines are drawn as a guide to the eye.

The position of this peak reveals a remarkable red shift from 307 to 296 cm^{-1} with increasing x , as well as the line broadening and monotonic increase in intensity (Fig. 9). Furthermore, an additional low-frequency component at 256 cm^{-1} appears to be visible for the $x = 0.5$ and $x = 0.6$ samples. The amplitude of this mode is roughly 3 % compared to that for the 300 cm^{-1} feature. Structural implications of the Raman data will be discussed in the next sections taking into account the mercury sulphide dimorphism.

3.5 Mercury sulphide dimorphism and Raman spectra of glasses

Mercury sulphide exists in two polymorphic modifications at ambient pressure: (a) red trigonal cinnabar α -HgS (space group $P3_121$), stable from low temperatures up to $344\text{ }^\circ\text{C}$, and (b) black cubic metacinnabar β -HgS (space group $F\bar{4}3m$), stable at higher temperatures. The crystal structure of cinnabar is very unusual for the III-V and II-VI semiconductors which usually exhibit either cubic zinc-blende or hexagonal wurtzite structures. Instead, α -HgS consists of $(\text{HgS}_{2/2})_n$ helical or zig-zag chains, six atoms to a

turn, Fig. 10(a).⁵⁴ The Hg-S-Hg nearest-neighbour (NN) angles are $\approx 104^\circ$, while the -S-Hg-S- NN bonds make a nearly straight-angle ($\approx 173^\circ$). The two-fold coordinated Hg and S species reveal the average interatomic intrachain distance of 2.38 Å; the nearest interchain Hg-S contacts are longer, ≈ 3.10 and ≈ 3.27 Å.⁵⁴



Fig. 10 (a) Helical or zig-zag $(\text{HgS}_{2/2})_n$ chains in trigonal cinnabar α -HgS,⁵⁴ (b) $\text{HgS}_{4/4}$ and $\text{SHg}_{4/4}$ tetrahedra in cubic metacinnabar β -HgS,³⁴ (c) suggested cinnabar-like, and (d) metacinnabar-like motifs in the $\text{HgS-As}_2\text{S}_3$ glasses.

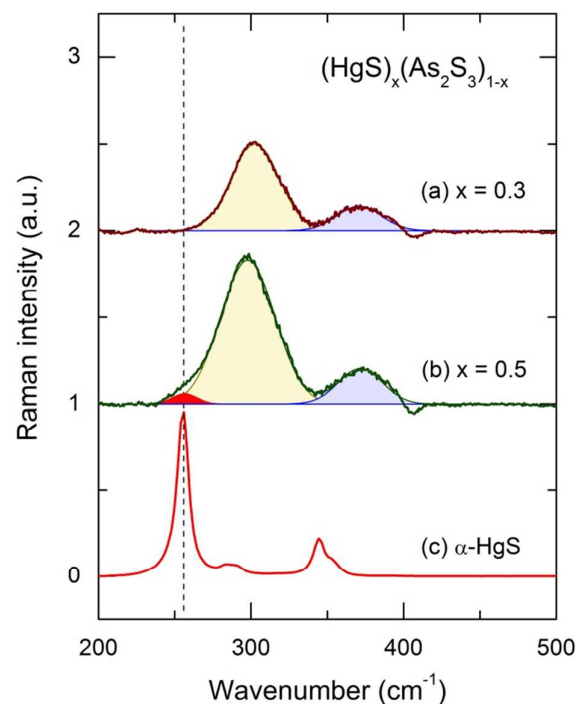


Fig. 11 Difference Raman spectra for (a) $x = 0.3$ and (b) $x = 0.5$ glasses $\text{HgS-As}_2\text{S}_3$; (c) typical Raman spectrum for trigonal cinnabar α -HgS. The dashed line at 256 cm^{-1} corresponds to the most intense A_1 symmetric mode in vibrational spectra of trigonal cinnabar.^{55,56}

The cubic zinc-blende structure of metacinnabar is shown in Fig. 10(b).³⁴ Both mercury and sulphur atoms are 4-fold coordinated by heteropolar neighbours forming a nearly perfect tetrahedron, $\angle\text{S-Hg-S} = \angle\text{Hg-S-Hg} = 109.5^\circ$. The Hg-S NN distance in metacinnabar is slightly longer, ≈ 2.54 Å, resulting in a lower density of β -HgS compared to α -HgS (7.70 vs. 8.17 g cm^{-3}). The $\text{HgS}_{4/4}$ or $\text{SHg}_{4/4}$ tetrahedra share their corners, evidenced by the Hg-Hg or S-S second neighbour distance of ≈ 4.14 Å. Consequently, two different mercury sulphide local environments could appear in disordered glass network: (A) Hg-S chains and/or (B) tetrahedral $\text{HgS}_{4/4}$ -related motifs.

The difference Raman spectra of selected $(\text{HgS})_x(\text{As}_2\text{S}_3)_{1-x}$ glasses, shown in Fig. 11 together with the Raman data for α -HgS, reflect both similarities and differences compared to crystalline mercury sulphide. Trigonal cinnabar over the $200\text{-}600 \text{ cm}^{-1}$

spectral range is characterised by the most intense A_1 mode at 256 cm^{-1} and two weak LO/TO doublets of the E-modes at $290/283\text{ cm}^{-1}$ and $354/345\text{ cm}^{-1}$, respectively.^{55,56} The observed broad features in the difference spectra of glasses at 300 and 370 cm^{-1} are reminiscent of the A_1 and more intense high-frequency E-mode in α -HgS even though they are blue-shifted by ≈ 40 and $\approx 20\text{ cm}^{-1}$. The higher frequency of the Hg-S stretching in the glass can be related to hybrid Hg-S chain/As-S pyramidal motifs, schematically shown in Fig. 10(c). There are two possible and complementary reasons of the blue shift. First, the hybrid network implies the reduced average atomic mass of an Hg-related oscillator, $\langle m_{\text{Hg}} \rangle \propto (k_1 m_{\text{Hg}} + k_2 m_{\text{As}} + k_3 m_{\text{S}})$, where k_i is the weighting factor for the i -species, thus increasing the vibration frequency, $\omega \propto \langle m_{\text{Hg}} \rangle^{-1/2}$. The asymmetric bonding, $-\text{Hg}-\text{S}-\text{As}=\text{}$, can also change vibrational force constants. Alternatively or additionally, the isolated $(\text{HgS}_{2/2})_n$ helical chains in the hybrid network are supposed to be weakly interacting in contrast to cinnabar, where the nearest interchain Hg-S contacts ($\approx 3.10\text{ \AA}$) appear to be significantly shorter than the sum of the van der Waals radii for mercury (2.05 \AA) and sulphur (1.80 \AA).⁵⁷ The strong interchain interactions in α -HgS weaken the intrachain bonding and decrease the Hg-S stretching frequencies compared to isolated/weakly interacting $(\text{HgS}_{2/2})_n$ chains.

The role of interchain interactions on the vibrational and structural properties was extensively studied for trigonal selenium, t -Se, and tellurium, t -Te, consisting of helical $(\text{Se}_{2/2})_n$ or $(\text{Te}_{2/2})_n$ chains.^{58,59} The confinement of isolated chalcogen chains in zeolites or aluminophosphates with one-dimensional channels resulted in remarkable changes of the vibrational spectra and intrachain distances.⁶⁰⁻⁶² The most intense A_1 symmetric stretching mode of t -Te was shifted from 122 cm^{-1} to 164 cm^{-1} ,^{60,63} i.e., $+42\text{ cm}^{-1}$; the weaker E modes appeared to be less sensitive to the interchain interactions.⁶⁴ Similar effect was observed for Te nanoparticles in ultra-thin layers with a typical thickness of 5 \AA also consisting of weakly interacting $(\text{Te}_{2/2})_n$ chains.⁶⁵ The Te-Te interatomic distance in these chains was reduced from the bulk t -Te value of 2.835 \AA to 2.792 \AA with a simultaneous increase of the intrachain force constant and characteristic Einstein temperature by $\approx 30\%$.

The opposite trend, a softening of the lattice vibration modes, was observed in trigonal Se and Te under high pressure^{66,67} caused by increasing interchain interactions and decreasing strength of the intrachain bonding. The A_1 stretching mode in t -Te exhibits again a remarkable red shift from 122 cm^{-1} (ambient pressure) to 105 cm^{-1} (4 GPa) while the two degenerated E modes appear to be rather insensitive to pressure changes.

Consequently, the observed blue-shift in the difference spectra of the $(\text{HgS})_x(\text{As}_2\text{S}_3)_{1-x}$ glasses compared to α -HgS, Fig. 11, is consistent with the hybrid chain/pyramidal network. The $(\text{HgS})_x(\text{As}_2\text{S}_3)_{1-x}$ glass density and mean atomic volume, Fig. 2, show a denser packing for α -HgS in comparison to hypothetical HgS glass at $x = 1$, whose extrapolated density (-19%) and atomic volume ($+12\%$) suggest more distant $(\text{HgS}_{2/2})_n$ neighbouring chains. Nevertheless, the quantitative analysis of the vibrational spectra needs a DFT modelling of isolated oligomeric Hg-S chains. Previously, the DFT

modelling of small chalcogen clusters was found to be an efficient tool to describe the vibrational, electronic and structural properties of confined chalcogen species.^{68,69}

3.6 Structural model: mercury sulphide chains vs. $\text{HgS}_{4/4}$ tetrahedra

Figure 12 shows the DFT Raman spectra of oligomeric Hg_2S_3 and Hg_4S_5 chain fragments; the optimised geometry parameters are collected in Table 1. First of all, we should note shorter Hg-S interatomic distances in the isolated chains, 2.35 Å, compared to those in bulk α -HgS, 2.38 Å. The Hg-S-Hg and S-Hg-S angles are rather similar in the two contrasting cases. The most intense symmetric in-phase Hg-S stretching in the Hg_2S_3 oligomer appears at 306 cm^{-1} , the symmetric out-of-phase and asymmetric in-phase Hg-S stretching modes are observed at 325 and 355 cm^{-1} , respectively. The stretching vibrations in Hg_2S_3 are visualised in SM1-SM3 movies (ESI). The symmetric in-phase Hg-S stretching shifts to lower frequencies with increasing chain length and shows a maximum at 296 cm^{-1} for the Hg_4S_5 oligomer, Fig. 12(b).

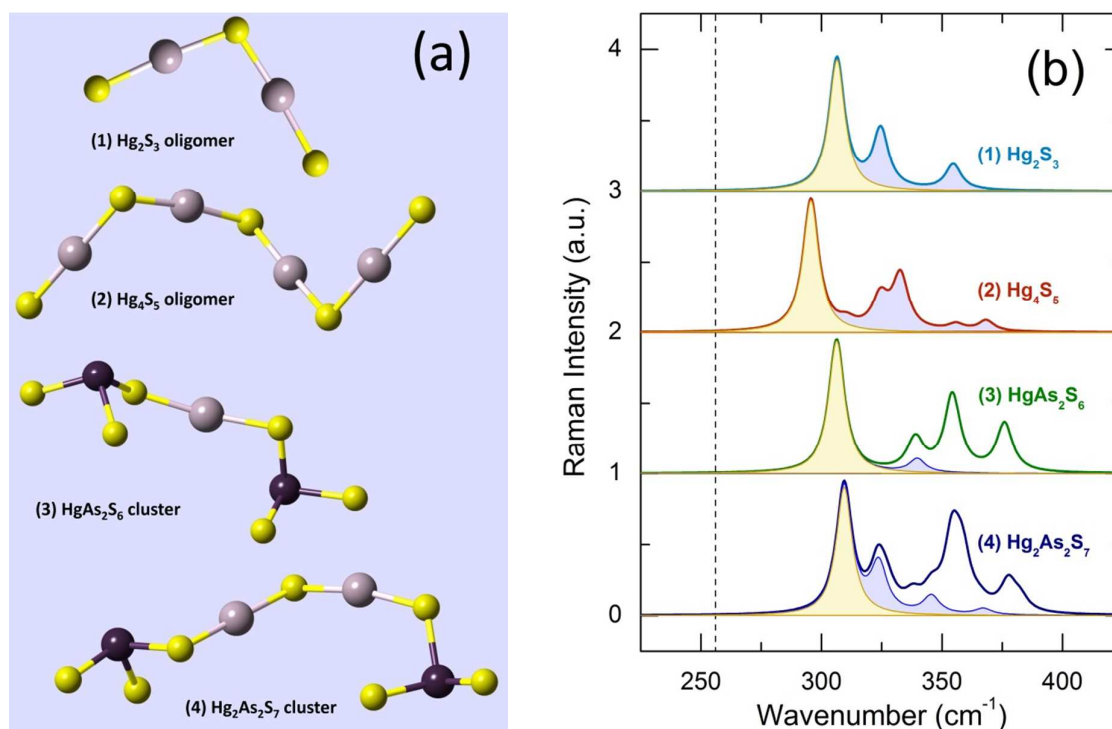


Fig. 12 (a) Schematic representation of oligomeric and hybrid units used for DFT modelling; the terminal hydrogen species are omitted; (b) the DFT Raman spectra in the stretching domain for (1) Hg_2S_3 and (2) Hg_4S_5 oligomers, (3) HgAs_2S_6 and (4) $\text{Hg}_2\text{As}_2\text{S}_7$ hybrid clusters, plotted using fixed FWHM of 8 cm^{-1} . The hydrogen-related modes are removed from the spectra. The highlighted features in yellow at $296 \leq \omega \leq 309 \text{ cm}^{-1}$ correspond to symmetric in-phase Hg-S stretching in $(\text{HgS}_{2/2})_n$ chain fragments. The highlighted features in blue represent symmetric out-of-phase and/or asymmetric Hg-S stretching. The dashed line at 256 cm^{-1} shows the A_1 peak position in trigonal cinnabar α -HgS.

A single $\text{HgS}_{2/2}$ chain fragment inserted between two adjacent $\text{AsS}_{3/2}$ pyramids or HgAs_2S_6 hybrid cluster, Fig. 12(a), conserves both the bulk value of the Hg-S distances, 2.38 Å, and related Hg- ($\angle\text{S-Hg-S} = 178^\circ$) and S-centred ($\angle\text{Hg-S-As} = 104^\circ$) bond angles (Table 1). Nevertheless, the most intense symmetric Hg-S stretching mode in HgAs_2S_6 is also blue-shifted to 306 cm^{-1} from the A_1 mode in $\alpha\text{-HgS}$ at 256 cm^{-1} . The next member of hybrid units' family, $\text{Hg}_2\text{As}_2\text{S}_7$, with two Hg-S chain fragments connecting the $\text{AsS}_{3/2}$ pyramids, reveals a nearly identical symmetric in-phase Hg-S stretching frequency compared to that in both HgAs_2S_6 and Hg_2S_3 units (Fig. 12). The symmetric out-of-phase Hg-S stretching at 324 cm^{-1} also remains invariant in the $n = 2$ hybrid, $\text{Hg}_2\text{As}_2\text{S}_7$, with respect to the $n = 2$ oligomer, Hg_2S_3 . The optimised geometry of the $\text{Hg}_2\text{As}_2\text{S}_7$ cluster represents a mixture of that for HgAs_2S_6 and Hg_2S_3 , e.g. the Hg-S interatomic distance for the symmetric bonding, $-\text{Hg-S-Hg}-$, is 2.35 Å, while for the asymmetric one, $-\text{Hg-S-As}=\text{}$, appears to be 2.38 Å (Table 1). It should also be noted that the C_s symmetry of the $\text{AsS}_{3/2}$ pyramids³⁵ remains intact in the hybrid clusters with two longer (2.29 Å) and one short (2.25 Å) arsenic-sulphur bonds and two different sets of the S-As-S angles.

Table 1 Optimised geometry parameters (mercury-sulphur, $r_{\text{Hg-S}}$, and arsenic-sulphur, $r_{\text{As-S}}$, interatomic distances, and related bond angles) of oligomeric Hg-S and hybrid Hg-As-S clusters used in DFT modelling of vibrational properties, and the reference crystalline compounds^{35,54}

	$r_{\text{Hg-S}}$ (Å)	$\angle\text{S-Hg-S}$ (deg)	$\angle\text{Hg-S-Hg}$ (deg)	$r_{\text{As-S}}$ (Å)	$\angle\text{S-As-S}$ (deg)	$\angle\text{Hg-S-As}$ (deg)
Hg_2S_3^\S	2.35	178	101	-	-	-
Hg_4S_5^\S	2.35	179(1)	101	-	-	-
$\text{HgAs}_2\text{S}_6^\S$	2.38	178	-	2.24 # 2.29(1) ‡	104 # 97(1) ‡	104
$\text{Hg}_2\text{As}_2\text{S}_7^\S$	2.35 2.38(1) §	176	100	2.25(1) # 2.29(2) ‡	104 # 96(2) ‡	102(2)
$\alpha\text{-HgS}^{54}$	2.377(2)	173.1(10)	104.2(3)	-	-	-
$\text{c-As}_2\text{S}_3^{35}$	-	-	-	2.257(19) # 2.296(9) ‡	104.6(5) # 96(3) ‡	-

[§] The terminal protons in the formula are omitted

[#] 33% of the As-S distances or S-As-S bond angles

[‡] 67% of the As-S distances or S-As-S bond angles

^{||} Hg-S interatomic distance for symmetric $-\text{Hg-S-Hg}-$ bonding

[§] Hg-S interatomic distance for asymmetric $-\text{Hg-S-As}=\text{}$ bonding

The last digit(s) in parentheses corresponds to the mean-square deviation (MSD) of the average experimental or calculated values. The missing MSD for the calculated geometry parameters means either a single calculated value or a negligible difference between several nearly identical geometry parameters.

Resuming, the DFT modelling reproduces well HgS-related features in the Raman spectra of the mercury thioarsenate glasses. The results are consistent with the suggested hybrid chain/pyramidal network. First of all, we note the position of the most intense symmetric in-phase Hg-S stretching mode at $\approx 300 \text{ cm}^{-1}$, blue-shifted from 256 cm^{-1} for trigonal cinnabar α -HgS. The less intense symmetric out-of-phase Hg-S stretching seems to be unresolved in the difference spectra of the HgS-As₂S₃ glasses, Figs. 8(b) and 11, caused by a broad experimental FWHM of 25-40 cm^{-1} , Fig. 9(b), compared to 8 cm^{-1} in the DFT spectra, Fig. 12(b). The observed monotonic decrease of the Hg-S symmetric stretching frequency in the (HgS)_x(As₂S₃)_{1-x} glasses with increasing x from 307 to 296 cm^{-1} , Fig. 9(a), implies a gradual agglomeration of the (HgS_{2/2})_n chain fragments, *i.e.*, the average number of chain fragments n per AsS_{3/2} unit increases, with a corresponding decrease of the vibration frequency. Finally, in the glass-forming limit at $x \geq 0.5$, a small fraction of long and presumably aggregated (HgS_{2/2})_n chains, where $n \rightarrow \infty$, becomes vibrationally decoupled from the remaining glass network and exhibits characteristic A₁ symmetric Hg-S stretching at 256 cm^{-1} , Fig. 11(b).

The hybrid Hg-S chain/As-S pyramidal network is very unusual for metal chalcogenide glasses. Mercury's neighbours in the Periodic Table (Tl, Pb, Bi), exhibit rather high local coordination numbers in glasses and liquids: $3 \leq N_{\text{Tl-S}} \leq 6$ in amorphous and liquid Tl-S binaries,^{71,72} $4 \leq N_{\text{Pb-S}} \leq 6$ in lead thioarsenate and thiogermanate glasses,^{73,74} or $4 \leq N_{\text{Bi-Se}} \leq 7$ in liquid Bi-Se alloys.⁷⁵ However, none of thallium, lead or bismuth chalcogenides has a chain-like structure in crystalline form.

The two-fold coordination of mercury is also consistent with the observed decrease of glass transition temperatures with increasing x , Fig. 4, caused by a successive replacement of more rigid CS-AsS_{3/2} pyramids by flexible (HgS_{2/2})_n chains. However, we cannot exclude completely the presence of tetrahedral HgS_{4/4} units, Fig. 10(d), in the hybrid network. First, large $x = 0.5$ samples contain the metacinnabar traces, Fig. 1(b), assuming a small fraction of four-fold coordinated mercury exists in the glass. Second, a non-monotonic change in electronic transport properties, Fig. 6, and in particular the composition dependence of $E_{\sigma}(x)$ with a maximum at $x = 0.3$ can also be related to a competition between insulating cinnabar-like and semiconducting metacinnabar-like motifs. The conductivity parameters of quasi-binary PbS-As₂S₃ glasses^{37,41,42} exhibit monotonic changes since semiconducting PbS^{41,42} does not have a dielectric polymorph. Finally, our preliminary neutron and high-energy x-ray scattering experiments carried out for the HgS-rich glasses, Fig. 1(a,b), reveal that the mercury coordination number, $N_{\text{Hg-S}}$, is slightly higher than 2.

The presence of HgS_{4/4} tetrahedra in the glass is difficult to prove using the Raman data alone because of their presumably small population and comparable Hg-S stretching frequencies. In fact, the Raman spectra of α -HgS and β -HgS were found to be rather similar in the stretching region.^{55,56,70} The most intense vibration mode of metacinnabar at 247 cm^{-1} seems to be hardly distinguishable from the A₁ cinnabar mode at 256 cm^{-1} when the two related structural motifs are present in the glass. We should however

note a monotonic broadening of the 300 cm^{-1} Hg-S stretching mode in the glass with increasing x , Fig. 9(b), possibly indicating the appearance of tetrahedral units. A detailed high-resolution diffraction study, similar to that for Ge-S binaries,⁷⁶ is in progress to solve this structural puzzle.

4 Conclusions

The quasi-binary $(\text{HgS})_x(\text{As}_2\text{S}_3)_{1-x}$ glasses, $0 \leq x \leq 0.5$, have been synthesised and characterised using DSC, density, DC conductivity and Raman spectroscopy measurements. The presence of crystallites was verified using laboratory XRD, high-energy x-ray scattering and pulsed neutron diffraction. The Raman spectroscopy results and DFT modelling reveal that the mercury thioarsenate glasses form a hybrid Hg-S chain/As-S pyramidal network evidenced by Hg-S stretching modes at 300 and 370 cm^{-1} and a usual As-S spectral envelope centred at 340 cm^{-1} . The decreasing glass transition temperature from $197\text{ }^\circ\text{C}$ to $169\text{ }^\circ\text{C}$ is consistent with a gradual substitution of more rigid corner-sharing $\text{CS-AsS}_{3/2}$ pyramids by flexible $(\text{HgS}_{2/2})_n$ chain fragments. Nevertheless, the presence of a small fraction of $\text{HgS}_{4/4}$ tetrahedral units in the hybrid network cannot be excluded completely. A non-monotonic change in electronic transport properties of these insulating glasses (the room-temperature conductivity varies between 10^{-15} and $10^{-17}\text{ S cm}^{-1}$) and metacinnabar β -HgS traces detected using neutron diffraction in large $x = 0.5$ samples support the dual structural role of mercury.

Acknowledgments

The authors thank Dr. Jörg Neuefeind (Oak-Ridge National Laboratory, USA) and Dr. Chris Benmore (Argonne National Laboratory, USA) for their help with neutron diffraction and high-energy x-ray scattering measurements, respectively. SK thanks the Communauté d'agglomération of Saint-Omer (France) for financial support of his PhD thesis.

References

- 1 C. A. Angell, *Science*, 1995, **267**, 1924-1935.
- 2 *Insulating and Semiconducting Glasses*, ed. P. Boolchand, World Scientific, Singapore, 2000.
- 3 N. F. Mott and E. A. Davis, *Electronic Processes in Non-Crystalline Materials*, Clarendon Press, Oxford, 1979.
- 4 E. Bychkov, *Solid State Ionics*, 2009, **180**, 510-516.
- 5 E. R. Meinders, A. V. Mijiritskii, L. van Pieterse and M. Wuttig, *Optical Data Storage*, Vol. 4, Springer, Philips Research Book Series, 2006.

- 6 M. Wuttig and N. Yamada, *Nature Mater.*, 2007, **6**, 824-832.
- 7 T. Matsunaga, J. Akola, S. Kohara, T. Honma, K. Kobayashi, E. Ikenaga, R. O. Jones, N. Yamada, M. Takata and R. Kojima, *Nature Mater.*, 2011, **10**, 129-134.
- 8 P. G. Bruce, S. A. Freunberger, L. J. Hardwick and J.-M. Tarascon, *Nature Mater.*, 2012, **11**, 19-29.
- 9 A. Hayashi, K. Noi, A. Sakuda and M. Tatsumisago, *Nature Commun.*, 2012, **3**, 856, 1-5.
- 10 M. Miloshova, E. Bychkov, V. Tsegelnik, V. Strykanov, H. Klewe-Nebenius, M. Bruns, W. Hoffmann, P. Papet, J. Sarradin, A. Pradel and M. Ribes, *Sensors Actuators B*, 1999, **57**, 171-178.
- 11 M. Miloshova and E. Bychkov, *J. Phys. Soc. Japan*, 2010, **79A**, 173-176.
- 12 J. Sanghera and I. D. Aggarwal, *Infrared Fiber Optics*, CRC Press, Boca Raton, Florida, 1998.
- 13 A. R. Hilton and S. Kemp, *Chalcogenide Glasses for Infrared Optics*, McGraw-Hill, NY, 2010.
- 14 B. J. Eggleton, B. Luther-Davies and K. Richardson, *Nature Photonics*, 2011, **5**, 141-148.
- 15 M. R. Riley, P. Lucas, D. Le Coq, C. Juncker, D. E. Boesewetter, J. L. Collier, D. M. De Rosa, M. E. Katterman, C. Boussard-Plédel and B. Bureau, *Biotechnol. Bioeng.*, 2006, **95**, 599-612.
- 16 X. H. Zhang, Y. Guimond and Y. Bellec, *J. Non-Cryst. Solids*, 2003, **326-327**, 519-523.
- 17 C. Beichman, G. Gomez, M. Lo, J. Masdemont and L. Romans, *Adv. Space Res.*, 2004, **34**, 637-644.
- 18 H. Martijn, A. Gromov, S. Smuk, H. Malm, C. Asplund, J. Borglind, S. Becanovic, J. Alverbro, U. Halldin and B. Hirschauer, *Infrared Phys. Technol.*, 2005, **47**, 106-114.
- 19 Z. U. Borisova, *Glassy Semiconductors*, Plenum, New York, 1981.
- 20 A. Feltz, *Amorphous Inorganic Materials and Glasses*, VCH, Weinheim, 1993.
- 21 Liang Zhenhua and Cheng Jijian, *J. Non-Cryst. Solids*, 1991, **136**, 205-212.
- 22 M. Kassem, D. Le Coq, M. Bokova and E. Bychkov, *Solid State Ionics*, 2010, **181**, 466-472.
- 23 M. Kassem, D. Le Coq, M. Fourmentin, F. Hindle, M. Bokova, A. Cuisset, P. Masselin and E. Bychkov, *Mater. Res. Bull.*, 2011, **46**, 210-215.
- 24 M. J. Frisch, G. W. Trucks, H. B. Schlegel, G. E. Scuseria, M. A. Robb, J. R. Cheeseman, G. Scalmani, V. Barone, B. Mennucci, G. A. Petersson, H. Nakatsuji, M. Caricato, X. Li, H. P. Hratchian, A. F. Izmaylov, J. Bloino, G. Zheng, J. L. Sonnenberg, M. Hada, M. Ehara, K. Toyota, R. Fukuda, J. Hasegawa, M. Ishida, T. Nakajima, Y. Honda, O. Kitao, H. Nakai, T. Vreven, J. A. Montgomery, Jr., J. E. Peralta, F. Ogliaro, M. Bearpark, J. J. Heyd, E. Brothers, K. N. Kudin, V. N. Staroverov, R. Kobayashi, J. Normand, K. Raghavachari, A. Rendell, J. C. Burant, S. S. Iyengar, J. Tomasi, M. Cossi, N. Rega, J. M. Millam, M. Klene, J. E. Knox, J. B. Cross, V. Bakken, C. Adamo, J. Jaramillo, R. Gomperts, R. E. Stratmann, O. Yazyev, A. J. Austin, R. Cammi, C. Pomelli, J. W. Ochterski, R. L. Martin, K. Morokuma, V. G. Zakrzewski, G. A. Voth, P. Salvador, J. J. Dannenberg, S. Dapprich, A. D. Daniels, Ö. Farkas, J. B. Foresman, J. V. Ortiz, J. Cioslowski, and D. J. Fox, *Gaussian 09, Revision D.01*, Gaussian, Inc., Wallingford CT, 2009.

- 25 A. Cuisset, F. Hindle, J. Laureyns and E. Bychkov, *J. Raman Spectrosc.*, 2010, **41**, 1050–1058.
- 26 A. D. Becke, *J. Chem. Phys.*, 1993, **98**, 5648-5652.
- 27 C. Lee, W. Yang and R. G. Parr, *Phys. Rev. B: Condens. Matter Mater. Phys.*, 1988, **37**, 785-789.
- 28 D. Feller, *J. Comput. Chem.* 1996, **17**, 1571–1586.
- 29 K. A. Peterson, D. Figgen, E. Goll, H. Stoll and M. Dolg, *J. Chem. Phys.* 2003, **119**, 11113.
- 30 P. Masselin, D. Le Coq, A. Cuisset and E. Bychkov, *Opt. Mater. Express*, 2012, **2**, 1768-1775.
- 31 N. Mateleshko, V. Mitsa and A. Kikineshi, *Fizika A*, 1999, **8**, 17-24.
- 32 R. Boidin, Ph. D. Thesis, University of Littoral, Dunkerque, France, 2013.
- 33 *CRC Handbook of Chemistry and Physics*, 78th edition, ed. D. R. Lide, CRC Press, New York, 1997-1998.
- 34 D. Rodic, V. Spasojevic, A. Bajorek and P. Onnerud, *J. Magn. Magn. Mater.*, 1996, **152**, 159-166.
- 35 D. J. E. Mullen and W. Nowacki, *Z. Kristallogr.*, 1972, **136**, 48-65.
- 36 K. L. Bhatia, S. C. Katyal and A. K. Sharma, *J. Non-Cryst. Solids*, 1983, **58**, 27-34.
- 37 Z. U. Borisova, E. A. Bychkov and Yu. S. Tveryanovich, *Interaction of Metals with Chalcogenide Glasses*, St. Petersburg University Press, St. Petersburg, 1991.
- 38 E. Bychkov, M. Miloshova, D. L. Price, C. J. Benmore and A. Lorriaux, *J. Non-Cryst. Solids*, 2006, **352**, 63-70.
- 39 S. Tsuchihashi and Y. Kawamoto, *J. Non-Cryst. Solids*, 1971, **5**, 286-305.
- 40 F. Kyriazis, A. Chrissanthopoulos, V. Dracopoulos, M. Krbal, T. Wagner, M. Frumar and S. N. Yannopoulos, *J. Non-Cryst. Solids*, 2009, **355**, 2010-2014.
- 41 P. K. Bhat, K. L. Bhatia and S. C. Katyal, *J. Non-Cryst. Solids*, 1978, **27**, 399-409.
- 42 K. L. Bhatia, M. Singh and N. Kishore, *Thin Solid Films*, 1997, **293**, 303-309.
- 43 L. I. Berger, *Semiconductor Materials*, CRC press, New York, 1997.
- 44 A. K. Mahapatra and A. K. Dash, *Physica E*, 2006, **35**, 9-15.
- 45 A. T. Ward, *J. Phys. Chem.*, 1968, **72**, 4133-4139.
- 46 G. Lucovsky, *Phys. Rev. B: Condens. Matter Mater. Phys.*, 1972, **6**, 1480-1489.
- 47 E. I. Kamitsos, J. A. Kapoutsis, I. P. Culeac and M. S. Iovu, *J. Phys. Chem. B*, 1997, **101**, 11061-11067.
- 48 T. Wagner, S. O. Kasap, M. Vlcek, A. Sklenar and A. Stronski, *J. Non-Cryst. Solids*, 1998, **227-230**, 752-756.
- 49 P. Chen, C. Holbrook, P. Boolchand, D. G. Georgiev, K. A. Jackson and M. Micoulaut, *Phys. Rev. B: Condens. Matter Mater. Phys.*, 2008, **78**, 224208.
- 50 M. Frumar, A. P. Firth and A. E. Owen, *J. Non-Cryst. Solids*, 1983, **59-60**, 921-924.

- 51 K. Shimakawa, A. V. Kolobov and S. R. Elliott, *Adv. Phys.*, 1995, **44**, 475-588.
- 52 F. Kyriazis, S. N. Yannopoulos, *Appl. Phys. Lett.*, 2009, **94**, 101901.
- 53 A. Cuisset, unpublished results of the DFT modelling of vibrational properties in the As-S binary glass system, to be published elsewhere.
- 54 T. Schleid, P. Lauxmann and C. Schneck, *Z. Kristallogr., Suppl.*, 1999, **16**, 95.
- 55 R. Zallen, G. Lucovsky, W. Taylor, A. Pinczuk and E. Burstein, *Phys. Rev. B: Condens. Matter Mater. Phys.*, 1970, **1**, 4058-4070.
- 56 W. Imaino, C. T. Simpson, W. M. Becker and A. K. Ramdas, *Phys. Rev. B: Condens. Matter Mater. Phys.*, 1980, **21**, 634-642.
- 57 L. Pauling, *The Nature of the Chemical Bond*, Cornell University Press, Ithaca, NY, 1960; S. Batsanov, *Inorg. Mater.*, 2001, **37**, 871-885.
- 58 P. Cherin and P. Unger, *Inorg. Chem.*, 1967, **6**, 1589-1591.
- 59 P. Cherin and P. Unger, *Acta Crystallogr.*, 1967, **23**, 670-671; C. Adenis, V. Langer and O. Lindqvist, *Acta Crystallogr., Sect. C: Struct. Chem.*, 1989, **45**, 941-942.
- 60 V. N. Bogomolov, V. V. Poborchy, S. G. Romanov and S. I. Shagin, *J. Phys. C: Solid State Phys.*, 1985, **18**, L313-L317.
- 61 Y. Katayama, M. Yao, Y. Ajiro, M. Inui and H. Endo, *J. Phys. Soc. Japan*, 1989, **58**, 1811-1822.
- 62 P. Armand, M.-L. Saboungi, D. L. Price, L. Iton, C. Cramer and M. Grimsditch, *Phys. Rev. Lett.*, 1997, **79**, 2061-2064; I. L. Li, J. P. Zhai, P. Launois, S. C. Ruan and Z. K. Tang, *J. Am. Chem. Soc.*, 2005, **127**, 16111-16119.
- 63 R. Geick, E. F. Streigmeier and H. Auderset, *Phys. Status Solidi B*, 1972, **54**, 623-630; M. H. Brodsky, in *Light Scattering in Solids I*, ed. M. Cardona, 2nd edition, Springer, Berlin, 1983, pp. 208-252.
- 64 R. M. Martin, G. Lucovsky and K. Helliwell, *Phys. Rev. B: Condens. Matter Mater. Phys.*, 1976, **13**, 1383-1395.
- 65 H. Ikemoto and T. Miyanaga, *Phys. Rev. Lett.*, 2007, **99**, 165503; H. Ikemoto, A. Goyo and T. Miyanaga, *J. Phys. Chem. C*, 2011, **115**, 2931-2937.
- 66 W. Richter, J. B. Renucci and M. Cardona, *Phys. Status Solidi B*, 1973, **56**, 223-229.
- 67 C. Marini, D. Chermisi, M. Lavagnini, D. Di Castro, C. Petrillo, L. Degiorgi, S. Scandolo and P. Postorino, *Phys. Rev. B: Condens. Matter Mater. Phys.*, 2012, **86**, 064103.
- 68 S. Kohara, A. Goldbach, N. Koura, M.-L. Saboungi and L.A. Curtiss, *Chem. Phys. Lett.*, 1998, **287**, 282-288.
- 69 J. Akola and R. O. Jones, *Phys. Rev. B: Condens. Matter Mater. Phys.*, 2012, **85**, 134103.
- 70 W. Szuszkiewicz, B. Witkowska, M. Jouanne and M. Balkanski, *Mater. Sci. Forum*, 1995, **182-184**, 711-714.
- 71 L. Cervinka and A. Hruby, *J. Non-Cryst. Solids*, 1978, **30**, 191-209.
- 72 O. Uemura, T. Usuki, Y. Kameda and S. Iwabuchi, *J. Phys. Soc. Japan*, 1996, **65**, 2106-2111.

- 73 J. I. Petz, R. F. Kruh and G. C. Amstutz, *J. Chem. Phys.*, 1961, **34**, 526-529.
- 74 S. C. Rowland, F. Ritland, D. Haferburns and A. Bienenstock, Proc. 7th Int. Conf. Amorphous and Liquid Semiconductors, ed. W. E. Spear, Edinburgh, UK, 1977.
- 75 T. Usuki, Y. Shirakawa, S. Tamaki and S. Takeda, *J. Phys. Soc. Japan*, 1993, **62**, 148-154.
- 76 A. Bychkov, G. J. Cuello, S. Kohara, C. J. Benmore, D. L. Price and E. Bychkov, *Phys.Chem. Chem. Phys.*, 2013, **15**, 8487-8494.

Graphical abstract

Mercury thioarsenate glasses: a hybrid chain/pyramidal network

Mohammad Kassem,^{ab} Sohayb Khaoulani,^{ab} Arnaud Cuisset,^{ab} David Le Coq,^c

Pascal Masselin^{ab} and Eugene Bychkov^{ab}

Mercury thioarsenate glasses $(\text{HgS})_x(\text{As}_2\text{S}_3)_{1-x}$, $0.0 \leq x \leq 0.5$, form a hybrid $(\text{HgS}_{2/2})_n$ chain/ $\text{AsS}_{3/2}$ pyramidal network, highly unusual for metal chalcogenide glasses. This network is evidenced by Raman spectroscopy and DFT modelling and consistent with thermal properties. Nevertheless we cannot exclude completely the presence of a small fraction of $\text{HgS}_{4/4}$ tetrahedral units.

